PAPER

Check for updates

Effect of impregnation strategy on structural characteristics of Ce−Mn/Al₂O₃ and its catalytic ozonation of benzoic acid†

Shengjuan Shao, [iD] *[a] Ting Cheng,[b] Yifan Cheng[a] and Bingxin Chen[a]

Ce−Mn binary oxides supported on Al₂O₃ (Ce−Mn/Al₂O₃), with enhanced activity and stability for catalytic ozonation of benzoic acid, were synthesized using a facile impregnation method. The competitive synergetic effects between cerium and manganese significantly influenced the structural characteristics and catalytic performance of the catalysts depending on the impregnation sequence. Catalysts prepared *via* the one-step impregnation process exhibited a higher concentration of homogeneous Ce^{3+} species on the catalyst surface. This led to an increase in surface oxygen vacancies, thereby enhancing catalytic activity. In contrast, the two-step impregnation process resulted in fewer oxygen vacancies due to reduced competitive effects between cerium and manganese. Overall, the optimized Ce−Mn/Al₂O₃ catalysts demonstrated improved catalytic performance in ozonation reactions, highlighting the importance of impregnation method and calcination conditions in tailoring catalyst properties for enhanced activity and stability. Oxygen vacancies play a crucial role as active sites for ozone adsorption and dissociation into *O₂ and *O, facilitated by the reduction of Mn^{4+} to Mn^{3+} and the oxidation of Ce^{3+} to Ce^{4+}. This process forms an electron closed loop that maintains electron balance. The synergistic interactions between cerium and manganese enable rapid electron transfer between Ce^{4+} and Mn^{3+}, facilitating the regeneration of Ce^{3+} and Mn^{4+}. Due to the increase of the dual redox conjugate pairs and the surface reactive oxygen species, the catalytic ozonation activity and stability of Ce−Mn/Al₂O₃ was enhanced.

1. Introduction

Heterogeneous catalytic ozonation is considered to be one of the effective methods for the refractory organic pollutants in water.[1] Dhandapani *et al.*[2] conducted a comparative study on the catalytic ozonation capabilities of various metal oxides (Ag, Mn, Fe, Cu, Mg, Ce, Co, Cr, Ni, and V) supported on Al₂O₃. Among these, MnO₂/Al₂O₃ exhibited superior catalytic ozonation performance attributed to its excellent reducibility and the characteristics of p-type oxides facilitated the decomposition of O₃ into superoxide (˙O₂$^−$), enhancing the overall efficiency. Faria *et al.*[3] prepared mixed oxides-supported catalysts using the transition metal Mn and rare earth element Ce for catalytic ozonation of sulfanilic acid and aniline. The Ce−Mn mixed oxides demonstrated larger specific surface areas and stronger redox capacities compared to their single oxide counterparts. This resulted in significant improvements in the mineralization of sulfanilic acid and

aniline. The enhanced catalytic performance was primarily attributed to improved lattice oxygen mobility and increased surface reactive oxygen species, highlighting synergistic interactions between Ce and Mn.[4–6] Previous research has also indicated that the enhanced ozonation efficiency observed in Ce-containing catalysts is largely due to increased concentrations of Ce(III) and oxygen vacancies.[7–9] As is known to all, CeO₂ possesses a unique 4f orbital that is incompletely filled with electrons, enabling it to serve as an electron reservoir facilitating rapid conversion between Ce^{3+} and Ce^{4+}. This characteristic endows CeO₂ with high oxygen storage capacity and efficient oxygen transfer abilities. These findings underscore the importance of understanding metal oxide interactions and their impact on catalytic processes for water treatment applications.

Our previous work has also demonstrated that the redox pairs and oxygen vacancy had a synergetic effect on the catalytic ozonation of nitrobenzene wastewater by Ce−Mn/Al₂O₃.[10] However, the effects of preparation methods on the structural characteristics of Ce−Mn/Al₂O₃, especially the effects of impregnation sequence were not elucidated in our previous work. Zhu *et al.*[11] investigated the impact of impregnation sequence on the hydrothermal stability and NH₃-SCR activity of Ce−Nb/SnO₂ catalysts. They found that catalysts impregnated first with Nb followed by Ce exhibited enhanced synergy between Nb and Sn, showcasing the strongest

[a]Department of Chemistry and Chemical Engineering, Taiyuan Institute of Technology, Taiyuan, 030008, China. E-mail: shaosj_tit@163.com

[b]School of Chemistry and Chemical Engineering, North University of China, Taiyuan, Shanxi 030051, China

redox capability while also demonstrating superior structural stability and NH$_3$-SCR activity. In a similar vein, Ozcan *et al.*[12] compared the catalytic performance and stability of alumina-supported Co, W, Zr catalysts prepared using sequential impregnation and co-impregnation methods for biofuel production. Their results highlighted that the catalysts prepared *via* co-impregnation showed the highest bio-oil conversion rate and selectivity. These studies underscore the significant impact of impregnation methods, particularly impregnation sequence, on catalyst structure and catalytic activity. Further research in this area holds promise for optimizing catalyst design and performance in heterogeneous catalytic ozonation processes.

Benzoic acid (BA) is an aromatic organic compound widely employed as a food preservative in beverages, juices, cold foods, soy sauce, vinegar, and canned foods. It acts as a bacteriostatic agent, effectively inhibiting the growth of bacteria, molds, and fungi. Due to its resistance to biodegradation by traditional microbial methods,[13] effective treatment methods for benzoic acid wastewater include photocatalytic oxidation,[14,15] electrochemical oxidation,[16,17] and heterogeneous catalytic ozonation.[18–21] Qin *et al.*[18] investigated the catalytic performance of cerium oxide supported on N, S-doped activated carbon (Ce/ACNS) for the ozonation of benzoic acid. They attributed the superior activity of Ce/ACNS to increased surface electron density of N and S atoms, along with higher Ce(III) content on the surface. Fijołek *et al.*[19] studied CePO$_4$, CeO$_2$, and bifunctional CePO$_4$/CeO$_2$ nanocomposites for catalytic ozonation of benzoic acid in the presence of chlorides. Among these, CePO$_4$/CeO$_2$ exhibited the best ozonation recovery performance, and the improved reactivity was attributed to the synergistic interaction between CePO$_4$ and CeO$_2$ in the bifunctional nanocomposite. Franco Peláez *et al.*[20] utilized CeO$_2$ thin films to catalyze the ozonation of benzoic acid. They found that the oxidation of Ce^{3+} contributed to the formation of reactive oxygen species, facilitating high mineralization of benzoic acid. These findings underscore the diverse applications and effective mechanisms of cerium-based catalysts in advancing the treatment of benzoic acid wastewater through ozonation processes.

In this study, we evaluated the catalytic ozonation efficiency of Ce–Mn/Al$_2$O$_3$ using benzoic acid as the target pollutant. The main objectives were threefold: (1) to investigate the impact of different preparation methods, particularly the impregnation sequence, on the structural characteristics and catalytic properties of Ce–Mn/Al$_2$O$_3$. (2) To assess the catalytic activity and stability of Ce–Mn/Al$_2$O$_3$ in the degradation of benzoic acid through catalytic ozonation. (3) To elucidate the synergistic interactions between Ce and Mn binary oxides, focusing on how they enhance the overall catalytic performance. These objectives aimed to deepen our understanding of Ce–Mn/Al$_2$O$_3$ as a catalyst and its potential application in environmental remediation processes involving ozonation.

2. Experimental procedure

2.1 Catalyst preparation

The catalysts were prepared according to the impregnation methods including the one-step impregnation and two-step impregnation method. Ce–Mn/Al$_2$O$_3$ catalysts were synthesized with varying amounts of Mn and Ce at different Mn to Ce molar ratios (7 : 3, 3 : 1, 1 : 1, and 2 : 1).

For instance, the Ce–Mn/Al$_2$O$_3$ catalyst prepared *via* the one-step impregnation method had a total (Mn + Ce) content of 8.0 wt% and a Mn/Ce molar ratio of 7 : 3. Specifically, 0.34 g of Mn(CH$_3$COO)$_2$·4H$_2$O and 0.26 g of Ce(NO$_3$)$_3$·6H$_2$O (supplied by Shanghai Maclin Biochemical Technology Co., Ltd) were dissolved in 5 mL of deionized water. 2.0 g of γ-Al$_2$O$_3$ (∼2 mm) were added and ultrasonically impregnated for 60 minutes. The impregnated samples were then dried at 100 °C for 12 hours and calcined at temperatures ranging from 400 to 700 °C for 4 hours to obtain the Ce–Mn/Al$_2$O$_3$ catalyst.

For the two-step impregnation method, Ce–Mn(F)/Al$_2$O$_3$ was prepared by first impregnating Mn and then impregnating Ce; Ce(F)–Mn/Al$_2$O$_3$ was prepared by first impregnating Ce and then impregnating Mn. Mn/Al$_2$O$_3$ and Ce/Al$_2$O$_3$ were also prepared by the same method with the single metal content of 8.0 wt%.

2.2 Catalyst characterization

Transmission electron microscopy (TEM) images were acquired using an FEI Tecnai F20. X-ray diffraction (XRD) patterns were carried out on the Rigaku SmartLab powder diffractometer using a CuKα radiation source (λ = 1.541 Å) with the scanning range of 10–80°. The nitrogen adsorption/desorption Brunauer–Emmett–Teller (BET) tests were performed using the Micromeritics TriStar II surface area analyzer, and the average pore diameter of catalysts were calculated by the Barrett–Joyner–Halenda (BJH) method. X-ray photoelectron spectroscopy (XPS) spectra were determined on the Thermofisher K-Alpha spectrometer using an AlKα radiation source of 1487 eV with the spot size of 400 μm, and the binding energies were calibrated with reference to the C 1s line at 284.8 eV. Electron paramagnetic resonance (EPR) tests were performed on the Bruker A300 spectrometer at X-band (9.5 GHz) at 77 K. Raman spectra were obtained using a Horiba Scientific LabRAM HR Evolution spectrometer equipped with a laser emitting at an excitation wavelength of 514 nm.

2.3 Catalytic ozonation process

All experiments were performed in a glass column reactor with an effective volume of 1000 mL. Ozone was generated by the 3S–T3 ozone generator and dispersed into microbubbles by an aeration stick (Fig. S1†). Ozone concentration C_{O_3} was maintained at 7.5 mg L^{-1} with the flow rate V_{O_3} of 0.5 L min^{-1}. The concentration of benzoic acid wastewater (c_{BA}) was 50 mg L^{-1} which was analyzed by the TU-1950 UV-Vis spectrophotometer at the wavelength of 225 nm. The total organic carbon (TOC) was analyzed using the Aurora l030C TOC analyzer. The degradation rate of benzoic acid was estimated using eqn (1).

$$\eta_{BA}(\%) = \left(1 - \frac{c}{c_0}\right) \times 100 \tag{1}$$

where η_{BA} (%) is defined as the degradation rate of benzoic acid, c_0 and c (mg L^{-1}) are the concentration of benzoic acid at the initial and sampling time, respectively.

2.4 Methods of theoretical calculation

All calculations were performed using the DMol3 (Materials Studio 2018) based on the density functional theory (DFT).[22] The exchange and correlation interactions were calculated by generalized gradient approximation non-empirical function Perdew-Wang (GGA-PW91), the core electrons were calculated by the DFT semi-core pseudopotentials (DSPP) method, and the valence electrons were calculated by double-numerical plus polarization (DNP) function. The K point grid of Brillouin zone integration was set to $2 \times 2 \times l$, the cutoff radius was set to 4.2 Å, the convergence tolerance of self-consistent iteration was set to 2.0×10^{-6}, and the convergence accuracy of energy, maximum force and maximum displacement was set to 1.0×10^{-5} Ha, 0.002 Ha Å^{-1} and 0.005 Å, respectively. A four-layer periodic slab model containing twelve γ-Al$_2$O$_3$ units was obtained by cutting the γ-Al$_2$O$_3$ bulk along the (110) surface, fixing the bottom two layers and allowing the upper two layers to relax[23] and a 12 Å vacuum layer was added to the (110) surface along the z axis. A supported model of Ce–Mn cluster on Al$_2$O$_3$(110) surface (Ce–Mn/Al$_2$O$_3$(110)) was established by geometric configuration optimization.

The formation energy of oxygen vacancy on the surface of Ce–Mn/Al$_2$O$_3$(110) was calculated as follows:

$$E_{OV} = E_{Ce–Mn/Al_2O_3(110)–OV} + 1/2E_{O_2} - E_{Ce–Mn/Al_2O_3(110)}$$

The adsorption energy of O$_3$ at the oxygen vacancy of Ce–Mn/Al$_2$O$_3$(110) was as follows:

$$E_{ads} = E_{Ce–Mn/Al_2O_3(110)–O_3} - E_{O_3} - E_{Ce–Mn/Al_2O_3(110)–OV}$$

in which $E_{Ce–Mn/Al_2O_3(110)–OV}$ is the total energy of the Ce–Mn cluster supported on Al$_2$O$_3$(110) surface with the oxygen vacancy; $E_{Ce–Mn/Al_2O_3(110)}$ is the total energy of the interacting system of the Ce–Mn cluster with the Al$_2$O$_3$(110) surface; $E_{Ce–Mn/Al_2O_3(110)–O_3}$ is the total energy of the adsorption configuration of O$_3$ on Ce–Mn/Al$_2$O$_3$(110) surface with oxygen vacancy; and E_{O_3/O_2} is the energy of the isolated O$_3$/O$_2$ molecules.

3. Results and discussion

3.1 TEM analysis

Cerium and manganese oxides were successfully loaded onto the surface of γ-Al$_2$O$_3$, forming spherical (as shown in Fig. 1(a1 and a2)) and short rod-like structures. HRTEM lattice fringe images (Fig. 1(b1–b3)) further revealed specific crystal planes of cerium and manganese oxides. The lattice spacings of 0.255 nm corresponded to the (311) planes of Mn$_3$O$_4$ (JCPDS no. 13-0162). It has been verified that when manganese acetate is used as a precursor, MnO$_X$ is mainly the Mn$_3$O$_4$ phase.[24] Lattice spacings of 0.239 nm corresponded to the (211) planes of α-MnO$_2$ (JCPDS no. 44-0141), while lattice spacings of 0.312 nm corresponded to the (111) planes of fluorite-type CeO$_2$ (JCPDS no. 34-0394), indicating the presence of MnO$_2$ and CeO$_2$ on the catalyst surface.

3.2 Effect of catalyst preparation parameters on catalytic activity of Ce–Mn/Al$_2$O$_3$

The structural composition of the catalyst significantly influences its performance, particularly in relation to the molar ratio of metal precursors. Fig. 2(a) illustrates the structural and phase characteristics of synthesized Ce–Mn/Al$_2$O$_3$ catalysts at varying Mn/Ce molar ratios, analyzed via X-ray diffraction. In all samples, diffraction peaks (indicated by dashed lines) at approximately 37.60°, 39.49°, 45.86°, and 67.03° are attributed to the Al$_2$O$_3$ phase (JCPDS no. 10-0425). For catalysts with Mn/Ce ratios of 1:1 and 2:1, the predominant crystalline phase of manganese oxides is Mn$_3$O$_4$ (JCPDS no. 13-0162). With increasing Mn content, additional diffraction peaks associated with α-MnO$_2$ emerge at 18.11°, 28.84°, 37.52°, and 60.27° (JCPDS no. 44-0141) in catalysts with Mn/Ce ratios of 3:1 and 7:3, which is beneficial to improve the catalytic ozonation activity due to the best redox ability of Mn^{4+} species.[25] Ramsdellite-type MnO$_2$ is detected in catalysts with Mn/Ce ratios of 2:1 and 3:1. Additionally, diffraction peaks corresponding to Mn$_2$O$_3$ (JCPDS no. 33-0900) are observed in the Mn/Ce = 3:1 catalyst, indicating the presence of Mn^{3+} with oxygen vacancies.[26] The primary crystalline phase of cerium oxides is cerianite-type CeO$_2$ (JCPDS no. 34-0394), particularly evident in the Mn/Ce = 1:1 catalyst. A reduction in Ce content eliminates CeO$_2$ diffraction peaks, leaving only Ce$_2$O$_3$ (JCPDS no. 23-1048). The presence of Ce^{3+} indicates the existence of oxygen vacancies, which enhance catalytic ozonation activity.[27] Notably, no distinct CeO$_X$ diffraction peaks are detected in the Mn/Ce = 2:1 catalyst, whereas both Ce$_2$O$_3$ and MnO$_2$ peaks are evident in Mn/Ce = 7:3 catalysts, indicating potentially superior catalytic activity in subsequent ozonation processes. The catalytic performances of the catalysts follow the order Mn/Ce = 7:3 > 3:1 > 1:1 > 2:1 (Fig. S2†), suggesting optimal synergistic effects between Mn and Ce at a molar ratio of 7:3.

Appropriate calcination temperature is also important for the catalytic performance of catalysts. Too low calcination temperatures may lead to incomplete calcination of catalyst precursor, resulting in insufficient dispersion and formation of active sites, whereas excessively high temperatures can cause sintering of active sites.[28] For instance, at a calcination temperature of 400 °C, cerium oxides mainly consist of CeO$_2$ and Ce$_2$O$_3$, while manganese oxides are primarily Mn$_3$O$_4$. Upon increasing the calcination temperature to 600 °C, diffraction peaks associated with α-MnO$_2$ (JCPDS no. 44-0141) begin to appear. Comparatively, the intensity of Ce$_2$O$_3$ diffraction peaks increases in the catalyst calcined at 600 °C compared to that at 500 °C, indicating higher Ce^{3+} content, which makes for the improvement of catalytic ozonation activity. However, at 700 °C, the diffraction peaks of MnO$_2$ disappear, replaced by bixbyite α-Mn$_2$O$_3$.[29] The absence of Mn^{4+} results in decreased catalytic activity. Therefore, the catalytic performances of catalysts rank as follows: 600 °C > 500 °C > 400 °C > 700 °C, suggesting that the optimal calcination temperature is 600 °C.

The textural properties of catalysts, such as specific surface area and pore structure, significantly influence their catalytic performance, which correlates closely with metal loadings.
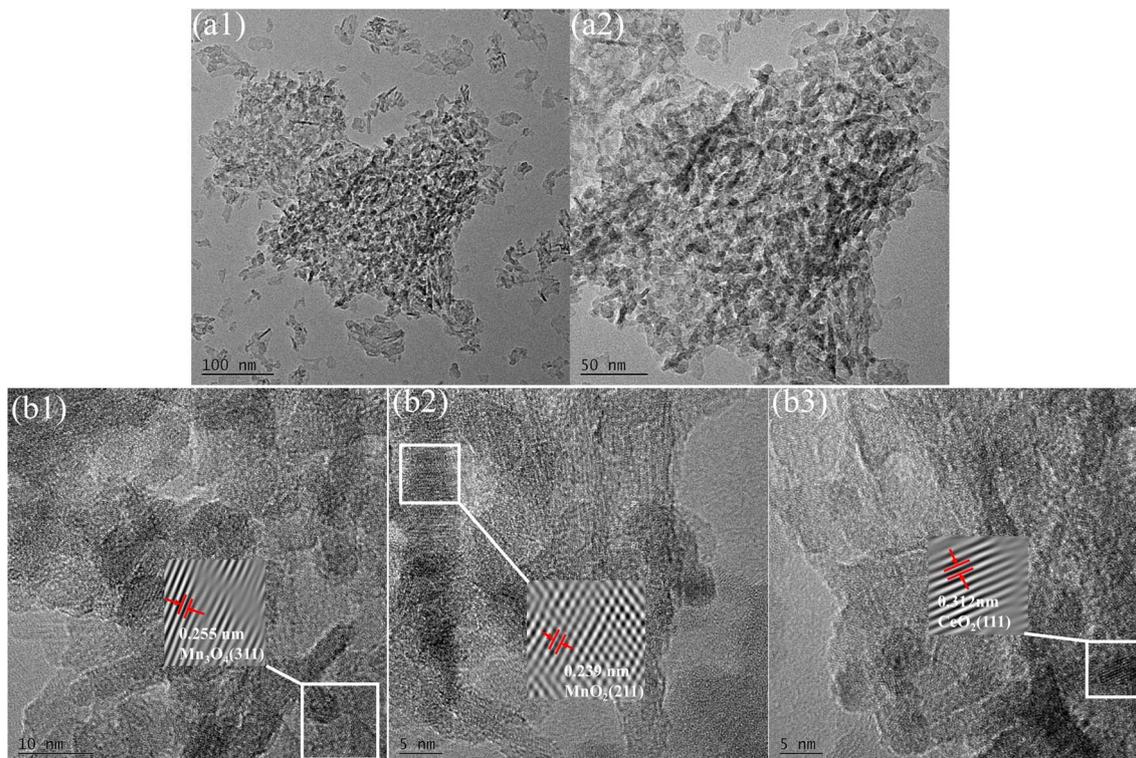
Fig. 1 TEM images (a1 and a2) and HRTEM images (b1–b3) of Ce−Mn/γ-Al$_2$O$_3$.

Insufficient loadings result in fewer active sites, whereas excessive ones can lead to surface clustering, thereby reducing catalytic ozonation performance.[28] As depicted in Fig. 3, the adsorption–desorption isotherms of Ce−Mn/Al$_2$O$_3$ synthesized with varying metal loadings exhibit similar type IV isotherms with a typical H3 hysteresis loop, albeit with slight alterations in pore distribution. Metal loadings on γ-Al$_2$O$_3$ have been observed to decrease specific surface area (S_{BET}) and pore volume (V_p) while increasing pore diameter (D_a) (Table S1†). It's noteworthy that there is minimal change in pore volume as metal loadings increase from 8% to 12%. This indicates that with the increase in metal loadings, more metal oxides are deposited onto the support surface. This phenomenon is particularly pronounced in the catalyst with %$_L$ = 12%, where the increase in S_{BET} can be attributed precisely to the presence of metal oxides supported on the γ-Al$_2$O$_3$ surface. The catalytic performances of the catalysts rank as follows: %$_L$ = 8% > 12% > 10% > 6%, suggesting that a metal loading of 8% is optimal.

3.3 Effect of impregnation sequence on catalytic ozonation activity of Ce–Mn/Al$_2$O$_3$

3.3.1 XRD patterns. The structural difference of Ce−Mn/Al$_2$O$_3$, Ce(F)–Mn/Al$_2$O$_3$ and Ce−Mn(F)/Al$_2$O$_3$ were also analyzed
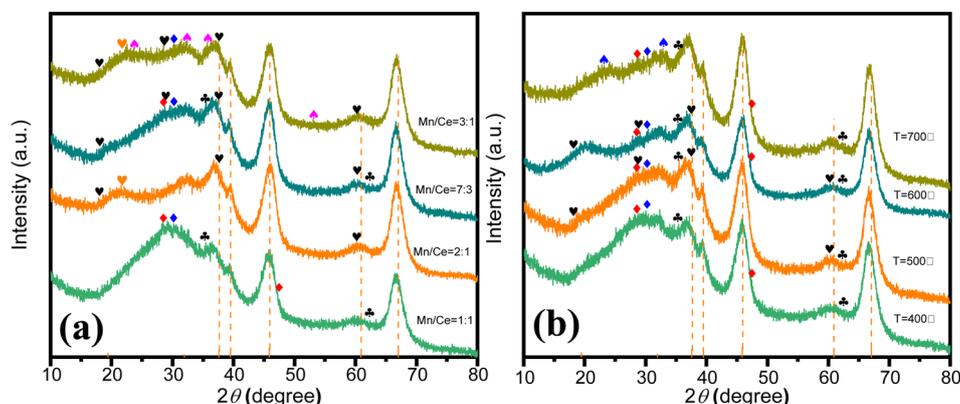

Fig. 2 XRD patterns of Ce−Mn/Al$_2$O$_3$ at different molar ratios of Mn/Ce (a) and different calcination temperatures (b). (♥ α-MnO$_2$, ♥ Ramsdellite, ♣ Mn$_3$O$_4$, ♠ Mn$_2$O$_3$, ♦ CeO$_2$, ♦ Ce$_2$O$_3$, ♠ bixbyite α-Mn$_2$O$_3$).
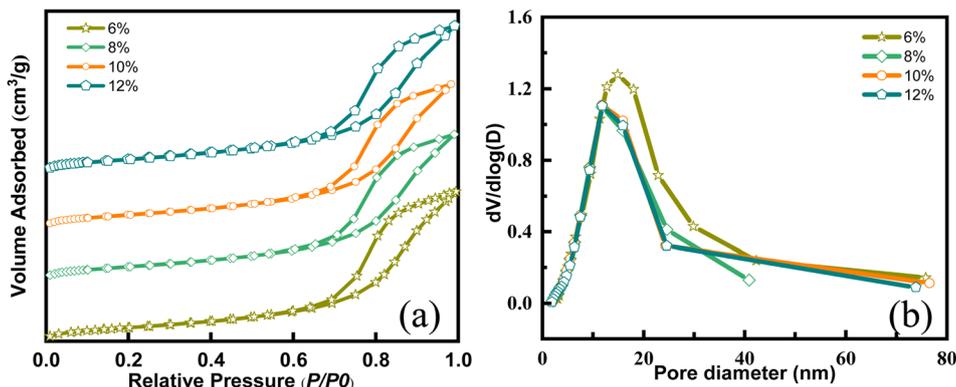
Fig. 3 N_2 adsorption and desorption isotherms (a) and pore size distribution curves (b) of Ce–Mn/Al$_2$O$_3$ with different metal loadings.
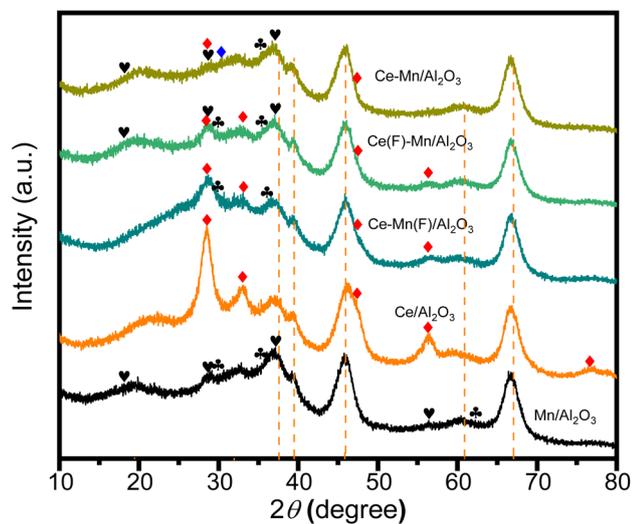

Fig. 4 XRD patterns of Ce–Mn/Al$_2$O$_3$, Ce(F)–Mn/Al$_2$O$_3$, Ce–Mn(F)/Al$_2$O$_3$, Ce/Al$_2$O$_3$ and Mn/Al$_2$O$_3$.

by XRD (Fig. 4) and the XRD patterns of Ce/Al$_2$O$_3$ and Mn/Al$_2$O$_3$ were used as a comparison. It can be seen that Ce–Mn/Al$_2$O$_3$ and Ce(F)–Mn/Al$_2$O$_3$ show similar XRD patterns to Mn/Al$_2$O$_3$, except that the diffraction peaks at 28.55° and 30.33° differ slightly from those of Mn/Al$_2$O$_3$ due to the introduction of Ce species. Both Ce–Mn/Al$_2$O$_3$ and Ce(F)–Mn/Al$_2$O$_3$ have the mixed crystal phase of MnO$_2$ and Mn$_3$O$_4$, but the peak intensity of MnO$_2$ in Ce(F)–Mn/Al$_2$O$_3$ is intensified. The impregnated manganese covers part of cerium and the interactions between manganese and cerium promotes the oxidation of manganese,[30] resulting in more MnO$_2$ on the Ce(F)–Mn/Al$_2$O$_3$ catalyst surface. In contrast, the competitive synergetic effects of cerium and manganese components promotes the surface dispersion of MnO$_2$ and the CeO$_2$, resulting in its weaker diffraction peak intensity. It has been reported that because the ionic radius of manganese ions (Mn^{3+}: 0.066 nm) is smaller than that of Ce^{4+} (0.092 nm), manganese ions can enter into the ceria lattice, weakening the diffraction peak intensity of CeO$_2$.[24,31] As for the Ce–Mn(F)/Al$_2$O$_3$, the first impregnation of Mn followed by Ce has a significant effect on the crystal structure of manganese.

The crystal phase of manganese in Ce–Mn(F)/Al$_2$O$_3$ is mainly Mn$_3$O$_4$ and the peak intensity of cerium oxide is also intensified. The impregnated cerium covers part of manganese and interacts with it, making it difficult to be further oxidized, mainly in the form of Mn$_3$O$_4$.[24,30]

3.3.2 XPS analysis. Fig. S3† and 5 shows the XPS survey and high-resolution scan spectra of Ce–Mn/Al$_2$O$_3$, Ce–Mn(F)/Al$_2$O$_3$ and Ce(F)–Mn/Al$_2$O$_3$ catalysts, further suggesting the elemental and chemical differences of Ce, Mn and O under different impregnation sequences. Table S2† also listed the surface atomic ratios of Ce, Mn and O elements of these samples. Since the ionic radius of Ce^{3+} is larger than that of Mn^{2+}, manganese is more inclined to be enriched in the pore interior than cerium, that is, the competitive impregnation occurred during the one-step impregnation. Therefore, the manganese content on the Ce–Mn/Al$_2$O$_3$ surface is the lowest. The two-step impregnation helps to improve the surface atomic ratio of Mn, and the Mn/Ce surface atomic ratio of Ce(F)–Mn/Al$_2$O$_3$ is the highest, which is close to 7 : 3.

Besides, the impregnation sequence has a great influence on the chemical states and relative percentage of elements on the catalyst surface (Table 1). For Mn 2p3/2 spectra, the fitting peaks at 640.4, 641.7 and 643.2 eV are ascribed to Mn^{2+}, Mn^{3+} and Mn^{4+}, respectively.[32–34] The satellite peak at ∼646 eV represents the existence of Mn^{2+}, and the shoulder peak at ∼643 eV represents the existence of Mn^{4+}.[35–37] As depicted in the Fig. 3(a), the ratios of Mn^{4+} to the sum of Mn^{4+}, Mn^{3+} and Mn^{2+} on Ce–Mn/Al$_2$O$_3$, Ce–Mn(F)/Al$_2$O$_3$ and Ce(F)–Mn/Al$_2$O$_3$ are 0.38, 0.34, and 0.40. It is consistent with the XRD results that the peak intensity of MnO$_2$ in Ce(F)–Mn/Al$_2$O$_3$ is intensified than that of Ce–Mn/Al$_2$O$_3$. Moreover, the ratios of Mn^{2+} are 0.30, 0.32 and 0.28, respectively. Combined with XRD analysis, the main crystal phase of manganese is Mn$_3$O$_4$ on Ce–Mn(F)/Al$_2$O$_3$, which is consistent with the increase of Mn^{2+} content in XPS results. That is, the first impregnation of Ce followed by Mn will increase the ratio of Mn^{4+}, while the first impregnation of Mn followed by Ce will increase the ratio of Mn^{2+}. The lowest content of Mn^{4+} on Ce–Mn(F)/Al$_2$O$_3$ is unfavorable for the improvement of catalytic activity.

For the Ce 3d spectra, it consists of 5 pairs of doublets, where u and v represent the Ce 3d5/2 and 3d3/2 spin–orbit splits,
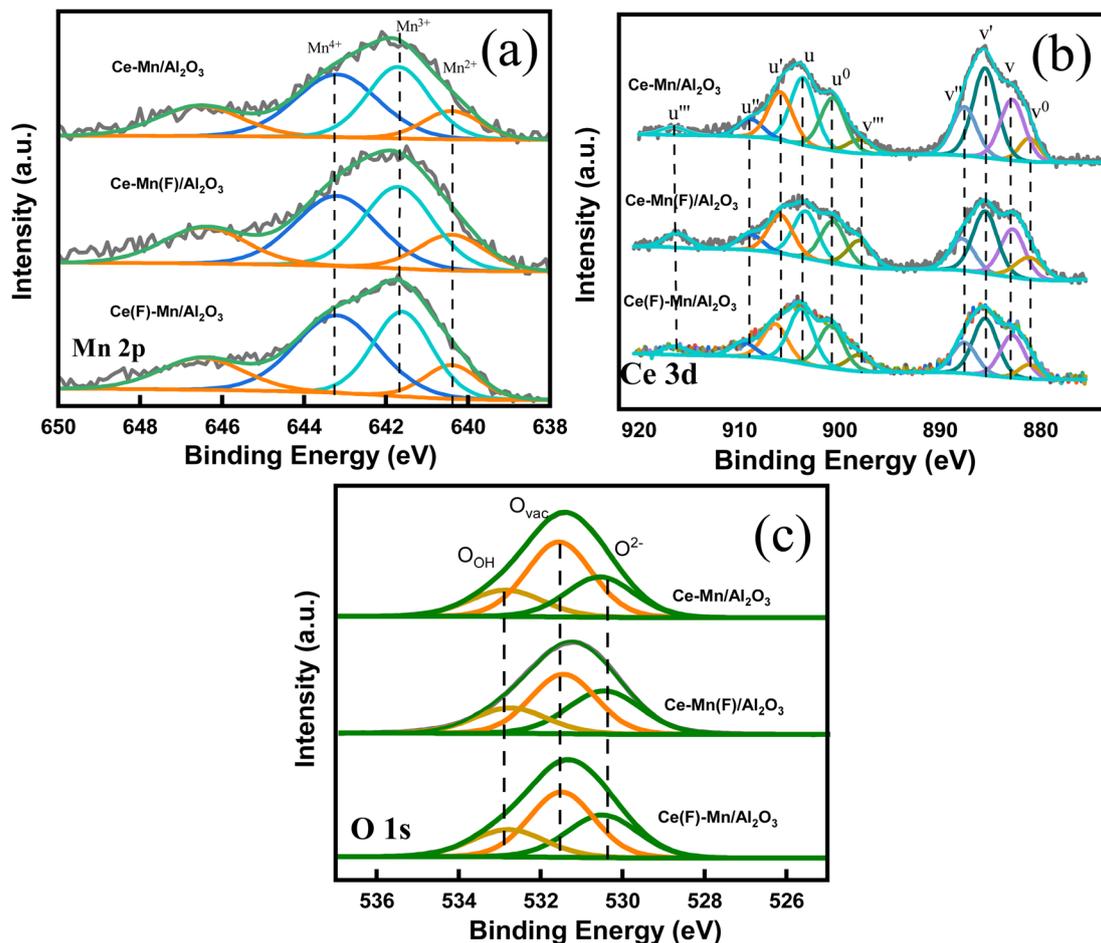
Fig. 5 High resolution Mn 2p (a), Ce 3d (b) and O 1s (c) XPS spectra of Ce–Mn/Al₂O₃, Ce–Mn(F)/Al₂O₃ and Ce(F)–Mn/Al₂O₃.

respectively. The peaks v (882.8 eV), v'' (887.5 eV), v''' (898 eV) are attributed to Ce^{4+} 3d3/2, and the peaks u (903.6 eV), u'' (909 eV), u''' (916.5 eV) are attributed to Ce^{4+} 3d5/2. The peaks v^0 (881.1 eV), v' (885.5 eV) are attributed to Ce^{3+} 3d3/2, and the peaks u^0 (900.7 eV), and u' (906 eV) are attributed to Ce^{3+} 3d5/2.[37,38] The ratios of Ce^{3+} to the sum of Ce^{4+} and Ce^{3+} on Ce–Mn/Al₂O₃, Ce–Mn(F)/Al₂O₃ and Ce(F)–Mn/Al₂O₃ are 0.52, 0.46, and 0.47, respectively. Obviously, the synergetic effects of Mn and Ce in the one-step impregnation promotes the formation of Ce^{3+}, while the two-step impregnation is adverse to the formation of

Ce^{3+}. The presence of Ce^{3+} can greatly increase the electron donor density and promote the formation of more oxygen vacancies due to the charge compensation.[39] By comparison, Ce–Mn/Al₂O₃ has the largest amount of Ce^{3+}, which is conclusive to the formation of more oxygen vacancies, thereby improving its catalytic ozonation activity.[33,40]

For O 1s spectra, the fitting peaks at 530.5 eV, 531.5 eV, 532.8 eV are ascribed to lattice oxygen (O^{2-}), surface atomic oxygen adsorbed on oxygen vacancies (O_{vac}) and surface hydroxyl groups or chemisorbed water (O_{OH}), respectively. The

Table 1 Binding energies and relative percentage of different chemical states of Mn, Ce and O of Ce–Mn/Al₂O₃, Ce–Mn(F)/Al₂O₃ and Ce(F)–Mn/Al₂O₃

Sample	O 1s (eV)				Mn 2p3/2 (eV)				Ce 3d (eV)		
	O_{OH}	O_{vac}	O^{2-}	O_{vac}/%	Mn^{4+}	Mn^{3+}	Mn^{2+}	Mn^{4+}/%	Ce^{4+}	Ce^{3+}	Ce^{3+}/%
Ce–Mn/Al₂O₃	532.8	531.5	530.5	51.24	643.2	641.7	640.4	37.72	$uu''u'''$ $vv''v'''$	u^0u' v^0v'	52.18
Ce–Mn(F)/Al₂O₃	532.8	531.5	530.5	43.75	643.2	641.7	640.4	34.49	$uu''u'''$ $vv''v'''$	u^0u' v^0v'	45.58
Ce(F)–Mn/Al₂O₃	532.8	531.5	530.5	45.77	643.2	641.7	640.4	40.5	$uu''u'''$ $vv''v'''$	u^0u' v^0v'	47.00
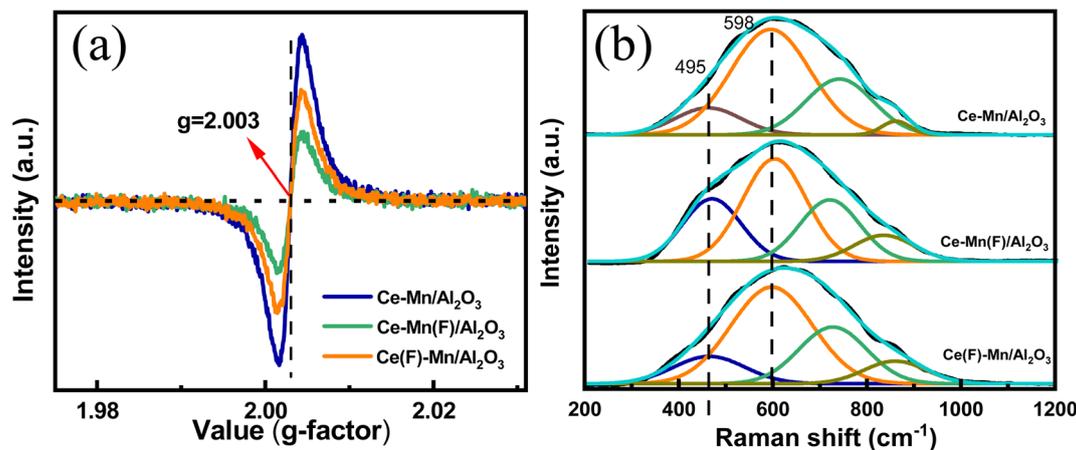
Fig. 6 EPR (a) and Raman (b) spectra of Ce−Mn/Al$_2$O$_3$, Ce−Mn(F)/Al$_2$O$_3$ and Ce(F)−Mn/Al$_2$O$_3$.
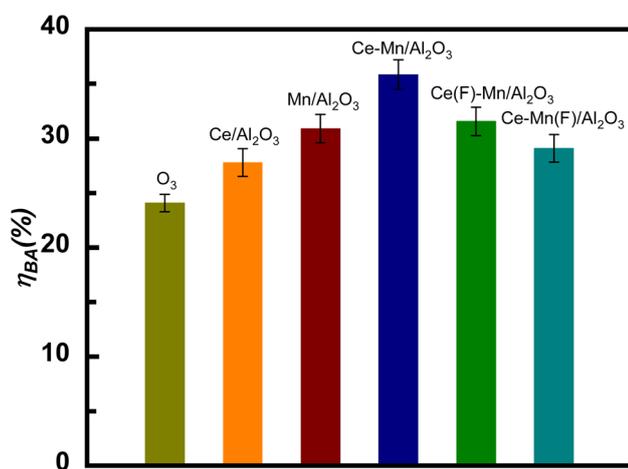

Fig. 7 Comparison of benzoic acid degradation efficiency between single and catalytic ozonation by Ce−Mn/Al$_2$O$_3$, Ce−Mn(F)/Al$_2$O$_3$ and Ce(F)−Mn/Al$_2$O$_3$ (V = 1000 mL, c_{BA} = 50 mg L^{-1}, m_s = 0.5 g L^{-1}, C_{O3} = 7.5 mg L^{-1}, time = 15 min).

ratios of O$_{vac}$ on Ce−Mn/Al$_2$O$_3$, Ce−Mn(F)/Al$_2$O$_3$ and Ce(F)−Mn/Al$_2$O$_3$ are 0.51, 0.44, and 0.46, respectively, indicating that there are abundant surface oxygen vacancies. It is well known that the content of oxygen vacancy in CeO$_2$ catalyst is closely related to the content of Ce^{3+},[41] and the content ordering of O$_{vac}$ in this study is exactly consistent with that of Ce^{3+}.

3.3.3 EPR analysis. To elucidate the influence of impregnation sequence on oxygen vacancy content and its subsequent impact on catalytic activity, EPR analysis was also conducted (Fig. 6(a)). A distinct signal at g = 2.003, characteristic of oxygen vacancy trapping electrons,[10,42] was observed on all catalysts. CeO$_2$ inherently possesses an oxygen defect structure due to its unsaturated surface atomic coordination, and the introduction of manganese further enhances the variation in Ce^{3+}/Ce^{4+}, thereby promoting oxygen defect formation. Specifically, the peak intensity follows the order of Ce−Mn/Al$_2$O$_3$ > Ce(F)−Mn/Al$_2$O$_3$ > Ce−Mn(F)/Al$_2$O$_3$, consistent with the sequence of Ce^{3+} and oxygen vacancy content (O$_{vac}$).

3.3.4 Raman analysis. Raman spectra also revealed variations in oxygen vacancies among different catalysts (Fig. 6(b)). It is known that the characteristic peak at 465 cm^{-1} corresponds to the symmetric Ce−O vibrational mode (F$_{2g}$) of CeO$_2$. In addition to this, the doped CeO$_2$ also exhibits a Raman peak near 595 cm^{-1}, which is attributed to the vibration peak of oxygen defects (D). All catalysts exhibited a broad band at 617 cm^{-1}, which can be deconvoluted into peaks at 465, 598, 729, 869 cm^{-1}, associated to F$_{2g}$, D, and characteristic peroxide peaks.[11,43] The ratio of peak area A$_{2g}$/A$_D$ reflects the relative abundance of oxygen vacancies. Specifically, the A$_{2g}$/A$_D$ ratios of Ce−Mn/Al$_2$O$_3$, Ce−Mn(F)/Al$_2$O$_3$ and Ce(F)−Mn/Al$_2$O$_3$ were 4.73, 1.80, 3.82, respectively, indicating that the concentration of oxygen vacancies followed the order of Ce−Mn/Al$_2$O$_3$ > Ce(F)−Mn/Al$_2$O$_3$ > Ce−Mn(F)/Al$_2$O$_3$, consistent with the EPR results.

In all, the competitive synergistic effects of cerium and manganese noticeably increased the oxygen vacancy content during the one-step impregnation process, whereas the absence of such competitive effects resulted in a decrease in oxygen vacancy content in the two-step impregnation processes.

3.3.5 Comparisons of catalytic activity. The catalytic performance of catalysts for the ozonation of benzoic acid are shown in Fig. 7. The degradation efficiency of benzoic acid (η_{BA}) in the catalytic ozonation by Ce/Al$_2$O$_3$, Mn/Al$_2$O$_3$, Ce−Mn/Al$_2$O$_3$, Ce(F)−Mn/Al$_2$O$_3$ and Ce−Mn(F)/Al$_2$O$_3$ were 27.8%, 30.9%, 35.9%, 31.6% and 29.1%, respectively, while the η_{BA} of the single ozonation was only 24.1% within 15 min. Under the synergetic effects of cerium and manganese, the catalytic ozonation activity of Ce−Mn/Al$_2$O$_3$ was greatly improved, and the η_{BA} of Ce−Mn/Al$_2$O$_3$ was 8.1% and 5.0% higher than that of Ce/Al$_2$O$_3$ and Mn/Al$_2$O$_3$, respectively. It is inferred from the XRD results that MnO$_2$ plays a dominant role in the catalytic ozonation performance, and its contribution is greater than that of CeO$_2$. When ceria is used as a single metal catalyst, its catalytic ozonation activity is not optimistic. Among the cerium oxides, the activity of Ce$_2$O$_3$ is more favorable. Therefore, the catalytic ozonation activity of Ce−Mn/Al$_2$O$_3$ was the highest, followed by Ce(F)−Mn/Al$_2$O$_3$, and then Ce−Mn(F)/Al$_2$O$_3$. In summary, the impregnation sequence had a great influence on the catalytic
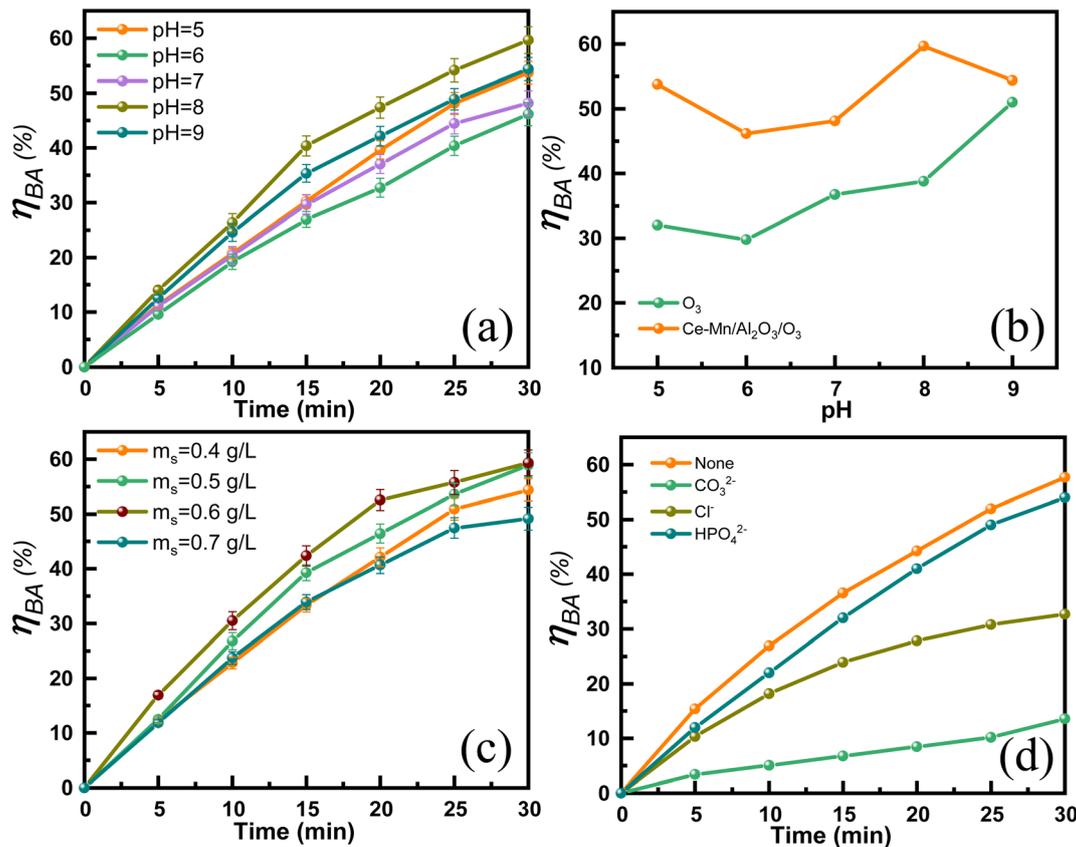
Fig. 8 Effect of pH (a) and (b), catalyst dosage (c) and anions (d) on the catalytic ozonation degradation efficiency of benzoic acid.

ozonation activity of catalysts, given that it can affect the synergetic effects of cerium and manganese, and then affect the metal valence state, oxygen vacancy, *etc.*

3.4 Catalytic ozonation activity and stability of Ce–Mn/Al$_2$O$_3$ on the degradation of benzoic acid

3.4.1 Effects of different parameters on the catalytic ozonation degradation efficiency of benzoic acid. Fig. 8(a)

shows the effects of solution pH on the ozonation efficiency of benzoic acid catalyzed by Ce–Mn/Al$_2$O$_3$. The highest degradation efficiency of BA was obtained at the solution pH = 8, and the η_{BA} reached 59.7% within 30 min. The solution pH can affect the electrification of hydroxyl groups on the catalyst surface and the decomposition rate constant of ozone. The point of zero charge (pH$_{PZC}$) of Ce–Mn/Al$_2$O$_3$ is 7.6 in this study. When the pH value is close to the pH$_{PZC}$, the hydroxyl groups on
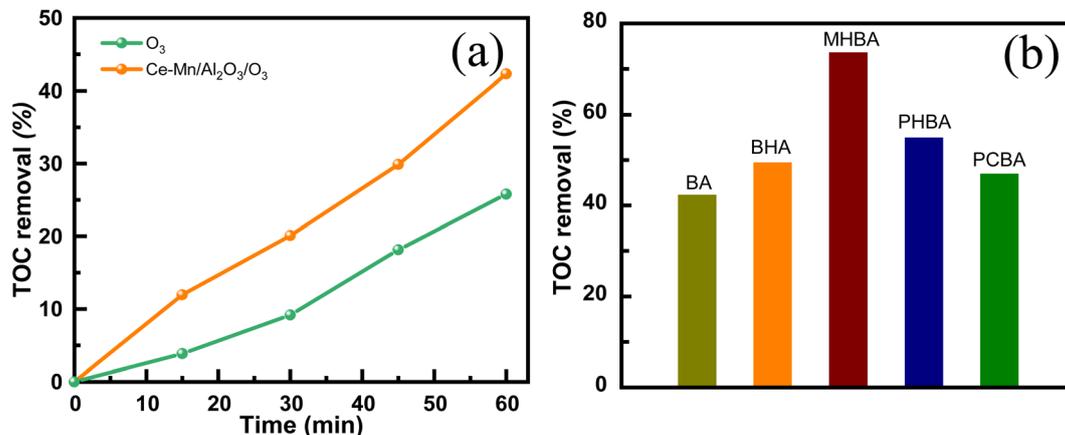

Fig. 9 TOC removal of benzoic acid solution in the single ozonation and catalytic ozonation (a) and TOC removal of benzoic acid derivatives during the catalytic ozonation (b) ($V = 1000$ mL, $c_0 = 50$ mg L^{-1}, $m_s = 0.5$ g L^{-1}, $C_{O_3} = 7.5$ mg L^{-1}, time = 60 min).

Table 2 Comparison of treatment efficiency with previous studies

Catalyst	C_{O_3}	m_s	c_{BA}/V_{BA}	Time	TOC removal efficiency	Ref.
CeO_2 film	15 mg min^{-1}	3 mg L^{-1}	115 mg L^{-1}/0.4 L	120 min	84%	20
Fe-shaving	60.8 mg min^{-1}	33.3 g L^{-1}	122 mg L^{-1}/1.5 L	90 min	56%	21
Mn/ZSM	20 mg min^{-1}	0.5 g L^{-1}	67.5 mg L^{-1}/0.5 L	30 min	75.4%	46
CeO_x/AC	—	0.5 g L^{-1}	50 mg L^{-1}/0.3 L	30 min	35%	18
$CePO_4$/CeO_2	—	0.2 g L^{-1}	2.9 mg L^{-1}/0.2 L	60 min	40%	19
Ce–Mn/Al_2O_3	3.75 mg min^{-1}	0.5 g L^{-1}	50 mg L^{-1}/1 L	60 min	42.3%	This study
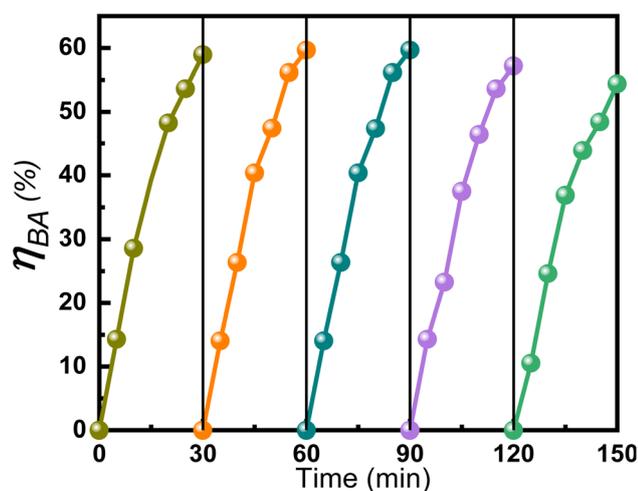
Fig. 10 The ozonation degradation efficiency of benzoic acid catalyzed by the reused Ce–Mn/Al_2O_3.

the catalyst surface are in a neutral state, which is conducive to accelerating the dissociation of ozone to hydroxyl radical (˙OH).[44] In addition, the alkaline condition also facilitates the initiation of ˙OH by the reaction of ozone with hydroxide ions. Thus, the η_{BA} increased with pH from 6 to 8 due to the enhanced indirect oxidation by the increased exposure of ˙OH. However, benzoic acid mainly exists in the anionic form when pH > pK_a (the pK_a value of benzoic acid is 4.21). When the solution pH = 9, an electrostatic repulsion will be generated between the negatively charged benzoic acid (pH > pK_a) and the negatively charged Ce–Mn/Al_2O_3 surface hydroxyl groups (pH > pH$_{PZC}$),[45] thus the η_{BA} began to decline. When pH < pHpzc, the surface hydroxyl groups are protonated, and the positively charged oxygen is not conducive to the adsorption and dissociation of ozone to ˙OH.[44] The degradation of BA is mainly ascribed to the direct oxidation by ozone in the acidic environment. When pH = 5, benzoic acid exists mainly in molecular form (pH ≈ pK_a), which favors the nucleophilic substitution of molecular ozone, resulting in a higher η_{BA} at pH = 5 than at pH = 6. A similar trend was observed in single ozonation. Fig. 8(b) compares the degradation efficiency of BA under different pH values for both single ozonation and catalytic ozonation. In an acidic environment, molecular ozone attacks benzoic acid through nucleophilic substitution, resulting in the formation of phenol. As benzoic acid dissociates, the nucleophilic substitution by ozone

weakens, and the degradation of BA increasingly relies on the attack by ˙OH. Consequently, starting at pH = 6, the degradation efficiency of BA in single ozonation increased with the rising pH, reaching a peak at pH = 9. This is attributed to the rapid self-decomposition of aqueous ozone into ˙OH in a strongly alkaline environment, which accelerates the degradation of BA. Overall, the degradation efficiency of catalytic ozonation is significantly higher than that of single ozonation.

Fig. 8(c) shows the effects of catalyst dosage on the catalytic ozonation efficiency of benzoic acid. The η_{BA} gradually increased from 54.4% to 59.3% with the catalyst dosage increases from 0.4 to 0.6 g L^{-1} due to the increased exposure of the surface reactive sites. Further increasing the catalyst dosage, the η_{BA} decreased. The possible reason maybe that high dosage of Ce–Mn/Al_2O_3 produces too much active species such as ˙OH and $O_2^{˙-}$, resulting in inactivation and self-quenching of active species.[45] Fig. 8(d) also shows the effects of common anions (CO_3^{2-}, Cl^-, HPO_4^{2-}, 10 mM) on the degradation efficiency of benzoic acid. The presence of anions resulted in a significant decrease of the degradation efficiency of benzoic acid, and its inhibitory effects followed the order of CO_3^{2-} > Cl^- > HPO_4^{2-}. Wang et al.[21] have proposed that the dominant reactive oxygen species for the degradation of BA is ˙OH. The stepwise hydroxylation of benzoic acid is the predominant reaction pathway, during which ˙OH react with the aromatic ring to form hydroxybenzoic acids, dihydroxy-benzoic acids and trihydroxy-benzoic acids.[46] CO_3^{2-} is known to have a strong scavenging effect on ˙OH, with the relatively high reaction rate constant ($k = 4.2 \times 10^8$ M^{-1} s^{-1}) and the η_{BA} significantly decreased from 57.7% to 13.6% in the presence of CO_3^{2-}. ˙OH can also be scavenged by Cl^- with the moderate reactivity ($k = 8.9 \times 10^7$ M^{-1} s^{-1}), resulting in a 25% reduction in η_{BA} in the presence of Cl^-.[47] It is inferred that due to the relatively low reactivity of HPO_4^{2-} with ˙OH, the η_{BA} was reduced by only 3.7% in the presence of HPO_4^{2-}.

3.4.2 Catalytic ozonation activity of Ce–Mn/Al_2O_3. Fig. 9(a) illustrates the TOC removal efficiency of benzoic acid solution in single ozonation and catalytic ozonation. The single ozonation removed only 25.8% of TOC within 60 min, whereas the catalytic ozonation by Ce–Mn/Al_2O_3 removed 42.3% of TOC from the benzoic acid solution, confirming the high ozonation activity of Ce–Mn/Al_2O_3. To further evaluate the ozonation activity of Ce–Mn/Al_2O_3 on refractory pollutants, we investigated its catalytic ozonation performance on representative benzoic acid derivatives, including salicylic acid (BHA), *m*-
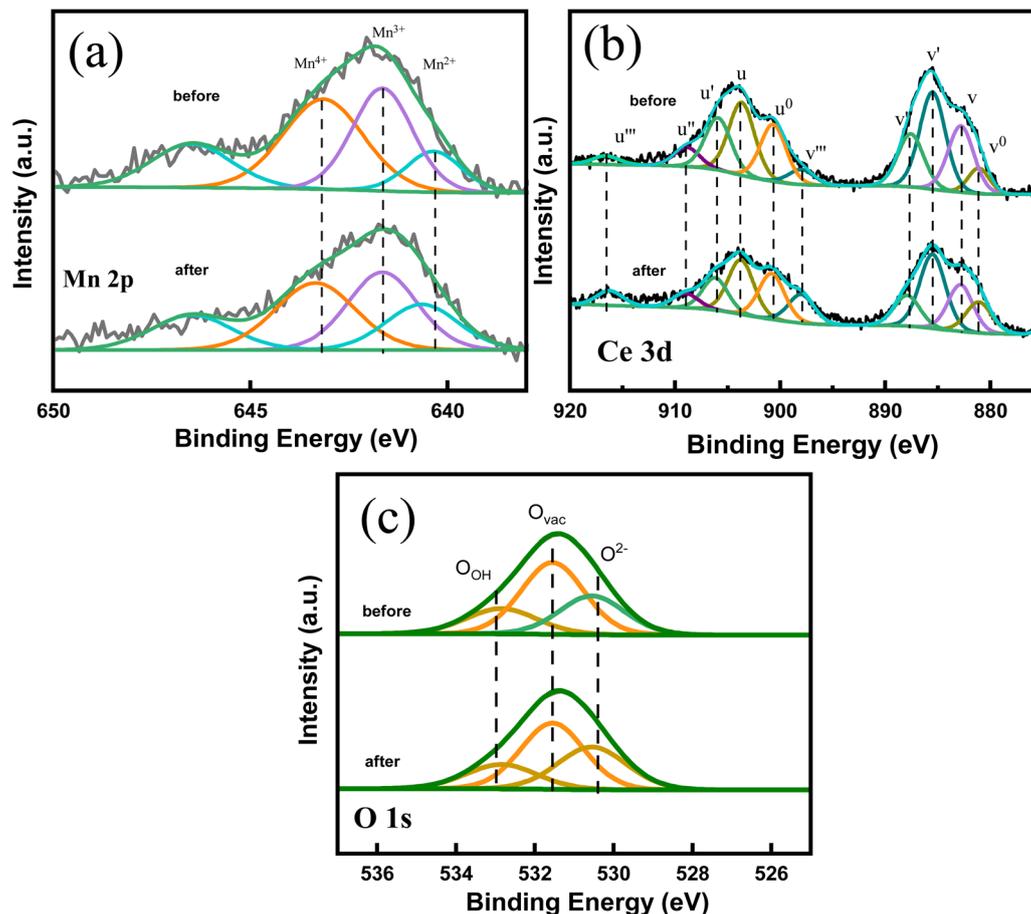
Fig. 11 High resolution Mn 2p (a), Ce 3d (b) and O 1s (c) XPS spectra of Ce−Mn/Al₂O₃ before and after use.

hydroxybenzoic acid (MHBA), *p*-hydroxybenzoic acid (PHBA), and *p*-chlorobenzoic acid (PCBA). As shown in Fig. 9(b), Ce–Mn/Al₂O₃ exhibited greater catalytic activity towards these benzoic acid derivatives, with the TOC removal efficiency following this order: MHBA > PHBA > BHA > PCBA > BA. Notably, the catalytic ozonation with Ce–Mn/Al₂O₃ removed 73.6% of TOC from the MHBA solution, and the TOC removal efficiency increased significantly with the introduction of the substituted group. Previous study has demonstrated that the introduction of –OH group on the benzene ring can change the stability of benzene ring and the reactivity with ozone due to the electron-donating effect, making it more prone to ring-opening reaction.[21] In the case of BHA, the *ortho*-effect appears to hinder the nucleophilic substitution of molecular ozone, resulting in poorer decarboxylation compared to other –OH substitutions. Conversely, the

meta-substitution in MHBA enhances nucleophilic addition by ˙OH and facilitates stepwise hydroxylation, promoting ring-opening reactions. For the substituted –Cl group, the electron-withdrawing effect also weakens the attack of molecular ozone on –COO⁻ group, with the observed TOC removal efficiency primarily resulting from the attack of ˙OH.[21,46]

Table 2 presents a comparison of the treatment efficiency of catalytic ozonation of BA with previous studies. The catalytic performance of Ce–Mn/Al₂O₃ in this study is at a moderate level compared with other reported catalysts, primarily due to the low ozone concentration and the large volume of the BA solution used. Notably, the spherical shape of the Ce–Mn/Al₂O₃ catalyst facilitates easier recovery from the aqueous solution compared to other powder-form catalysts.

Table 3 Binding energies and relative percentage of different chemical states of Mn, Ce and O of Ce−Mn/Al₂O₃ before and after use

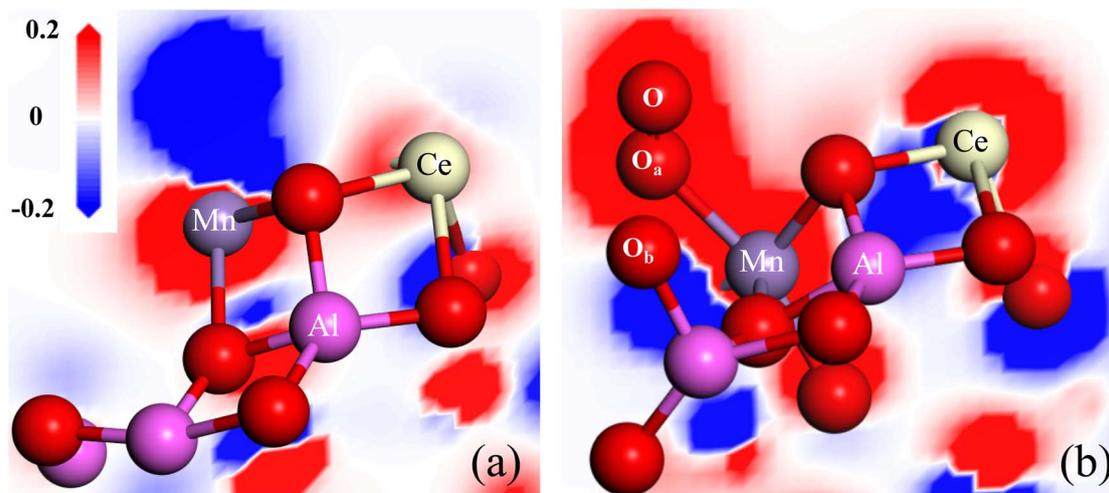| Sample	O 1s (eV)				Mn 2p3/2 (eV)				Ce 3d (eV)		
	O_{ads}	O_{vac}	O^{2-}	O_{vac}/%	Mn^{4+}	Mn^{3+}	Mn^{2+}	Mn^{4+}/%	Ce^{4+}	Ce^{3+}	Ce^{3+}/%
Before	532.8	531.5	530.5	51.24	643.2	641.7	640.4	37.72	$uu''u'''$ $vv''v'''$	u^0u' v^0v'	52.18
After	532.6	531.5	530.4	49.87	643.4	641.7	640.7	36.30	$uu''u'''$ $vv''v'''$	u^0u' v^0v'	45.66

Fig. 12 The differential charge density adjacent to the oxygen vacancy of Ce–Mn/Al$_2$O$_3$(110) surface before (a) and after (b) ozone adsorption.

3.4.3 Reusability and stability of Ce–Mn/Al$_2$O$_3$. The reusability of Ce–Mn/Al$_2$O$_3$ was investigated through the catalytic ozonation of benzoic acid by recycling Ce–Mn/Al$_2$O$_3$ catalysts and the results were shown in Fig. 10. The η_{BA} remained stable and increased slightly in the first three cycles due to the increased accessibility of surface-active sites. From the 4th cycle, the η_{BA} began to decline and decreased from 58.9% to 54.4% until the 5th cycle. The slight decrease in the catalytic ozonation activity of Ce–Mn/Al$_2$O$_3$ may be caused by the deactivation of the active sites due to the oxidation of ozone and reactive oxygen species, or the leaching loss of metal ions. Therefore, we also used XPS to analyze the chemical states and relative percentages of elements on the surface of Ce–Mn/Al$_2$O$_3$ after the fifth use (Fig. 11).

As shown in Table 3, the ratio of Mn^{4+} to the sum of Mn species decreases from 37.7% to 36.3%, while the ratio of Mn^{3+} increases from 32.2% to 36.5% after catalytic ozonation. The ratio of Ce^{3+} to the sum of Ce species decreases from 52.2% to 45.7% and the ratio of Ce^{4+} increases from 47.8% to 54.3%. The reduction of Mn^{4+} and the oxidation of Ce^{3+} occurred simultaneously in the catalytic ozonation process.[10,48–50] The significant increase in Ce^{4+} might result in an increase in the lattice oxygen, which is converted by the oxygen uptake at oxygen vacancies. Ozone molecule can also be adsorbed on the oxygen vacancy to form superoxide anion radicals,[51] and the surface hydroxyl groups can also be attacked by ozone molecule to form ozonide anion radicals.[52] As a result, the ratio of O$_{vac}$ decreases from 51.2% to 49.9% and the ratio of O$_{ads}$ also decreases from 20.3% to 18.2% after catalytic ozonation. In contrast, the ratio of O^{2-} increases from 28.5% to 31.9%. These results indicates that the active centers of catalytic ozonation of benzoic acid are mainly Mn^{4+}, Ce^{3+}, surface hydroxyl groups and oxygen vacancies. Although the inactivation and loss of the active sites occurred during the ozonation process, the synergetic interactions between cerium and manganese atoms enable the rapid electron transfer between Ce^{4+} and Mn^{3+} to promote the recovery of Ce^{3+} and Mn^{4+}:[53]

$$Ce^{4+} + Mn^{3+} \rightarrow Mn^{4+} + Ce^{3+} \qquad (2)$$
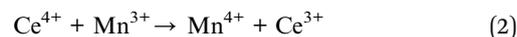
To illustrate this, we also studied the adsorption configuration of ozone on the active centers of Ce–Mn/Al$_2$O$_3$. The γ-Al$_2$O$_3$ structure is established and optimized according to the cell parameters provided by Digne *et al.*[54] The cell parameters are $a = 5.59$ Å, $b = 8.42$ Å, $c = 8.10$ Å and $\beta = 90.60°$. Since the (110) surface is considered to be the most exposed crystal surface of γ-Al$_2$O$_3$ (70–83%), the (110) surface is chosen as the representative of γ-Al$_2$O$_3$. The Ce–Mn/Al$_2$O$_3$ model is established by adsorption of the optimized Ce–Mn cluster on the surface of Al$_2$O$_3$(110). After optimization, Mn atom is bonded to O60, O61 and O62 with bond lengths of 2.30 Å, 1.90 Å and 2.04 Å respectively, and Ce atom is bonded to O23 and O15 with bond lengths of 2.38 Å, as shown in Fig. S4.†

The unsaturated coordination oxygen O64 can easily transfer electrons to Mn atom and release oxygen to form oxygen vacancy, given that its Mulliken charge is $-0.364|e|$ and its conformation is far away from the Ce–Mn/Al$_2$O$_3$(110) surface. The calculated oxygen vacancy formation energy E_{OV} is only 0.02 eV, indicating that the (110) surface of Ce–Mn/Al$_2$O$_3$ is very active to form oxygen vacancy defects. As shown in Fig. 12(a), with the formation of oxygen vacancy, the charge density around the oxygen vacancy drops sharply, resulting in a significant increase in the charge density around the Mn atom, forming an electron-rich center to maintain electrical neutrality. Meanwhile, there is also electron transfer between Mn and Ce atoms, and the charge density around Ce atom increase slightly due to the dual redox reaction of Mn^{3+}/Mn^{4+} and Ce^{4+}/Ce^{3+}.

When the ozone molecule is adsorbed on the oxygen vacancy of Ce–Mn/Al$_2$O$_3$(110) surface, it can be dissociated into *O$_2$ and bonded to the Mn atom. The O–O a bond length is 1.26 Å, which is exactly the same as that of O$_2$$^{\bullet-}$. At the same time, an *O atom is also formed and bonded to the Al atom (Fig. 12(b)), thus replenishing the released lattice oxygen. The dissociation energy of ozone on the oxygen vacancy of Ce–Mn/Al$_2$O$_3$(110)

surface is −34.18 kcal mol^{-1}, and the reaction energy barrier is only 1.616 kcal mol^{-1}. This process is very favorable both thermodynamically and kinetically. With the adsorption and dissociation of ozone on the oxygen vacancy, the charge density around Mn atom increases, while the charge density around Ce atom decreases, indicating that the adsorption of ozone on the oxygen vacancy is accompanied by the reduction of Mn^{4+} and the oxidation of Ce^{3+}. In a word, the oxygen vacancy acts as an effective active site for ozone adsorption and dissociation into *O$_2$ and *O, so the ratio of O$_{ads}$ increases correspondingly after catalytic ozonation, and this process also involves the dual redox reactions of Mn^{4+}/Mn^{3+} and Ce^{3+}/Ce^{4+} to form an electron closed loop and to maintain the balance of electron supply, which fully explains and supports our previous experimental results.

4. Conclusion

Ce–Mn binary oxides supported on Al$_2$O$_3$ with enhanced activity and stability for catalytic ozonation of benzoic acid have been obtained by one-step impregnation method. The different impregnation conditions especially impregnation sequence have a great influence on the structure and the catalytic ozonation performance of catalysts. The diffraction peaks of Ce$_2$O$_3$ and MnO$_2$ appeared in the catalyst with Mn/Ce = 7 : 3, and the calcination temperature of 600 °C enhanced the intensity of Ce$_2$O$_3$, which are favorable to the improvement of catalytic ozonation activity. Ce–Mn/Al$_2$O$_3$ demonstrated strong catalytic ozonation activity towards benzoic acid derivatives, achieving a TOC removal of 42.3% from benzoic acid and 73.6% from *m*-hydroxybenzoic acid solution within 60 min. The competitive synergetic effects of cerium and manganese in the one-step impregnation process promoted the dispersion of Ce component, resulting in more homogeneous Ce^{3+} species on the catalysts surface, which substantially increased the surface oxygen vacancies of catalysts, while the lack of competitive effects in the two-step impregnation process led to a decrease in oxygen vacancy content. Oxygen vacancies act as the effective active sites for ozone adsorption and dissociation to *O$_2$ and *O, accompanied with the reduction of Mn^{4+} to Mn^{3+} and the oxidation of Ce^{3+} to Ce^{4+}, to form an electron closed loop and maintain the balance of electron supply. The synergetic interactions between cerium and manganese also enable the rapid electron transfer between Ce^{4+} and Mn^{3+} to promote the recovery of Ce^{3+} and Mn^{4+}. Due to the synergetic effects, the catalytic ozonation activity and stability of Ce–Mn/Al$_2$O$_3$ was enhanced.

Data availability

The data supporting this article have been included as part of the ESI.†

Conflicts of interest

The authors declare no competing financial interest, and manuscript is approved by all authors for publication.

Acknowledgements

References

1 W. Chen, H. He, J. Liang, X. Wei, X. Li, J. Wang and L. Li, *J. Hazard. Mater.*, 2023, **443**, 130302.

2 B. Dhandapani and S. T. Oyama, *Appl. Catal., B*, 1997, **11**, 129–166.

3 P. C. C. Faria, J. J. M. Órfão and M. F. R. Pereira, *Catal. Commun.*, 2008, **9**, 2121–2126.

4 S. Gong, W. Wang, K. Chen, K. Xiao and Y. Yin, *J. Environ. Chem. Eng.*, 2022, **10**, 107571.

5 Z. Wu, G. Zhang, R. Zhang and F. Yang, *Ind. Eng. Chem. Res.*, 2018, **57**, 1943–1953.

6 W. Feng, F. He, X. Chen, B. Jiang, H. Wang and Z. Wu, *Chem. Eng. J.*, 2024, **488**, 150804.

7 Y. Ding, J. Wang, S. Xu, K.-Y. A. Lin and S. Tong, *Sep. Purif. Technol.*, 2018, **207**, 92–98.

8 F. Chen, X. Shen, Y. Wang and J. Zhang, *Appl. Catal., B*, 2012, **121–122**, 223–229.

9 J. Wang, X. Quan, S. Chen, H. Yu and G. Liu, *J. Hazard. Mater.*, 2019, **368**, 621–629.

10 S. Shao, Z. Li, J. Zhang, K. Gao, Y. Liu and W. Jiao, *Chem. Eng. Sci.*, 2022, **248**, 117246.

11 Y. Zhu, W. Shan, Z. Lian, J. Liu, Y. Zhang and H. He, *J. Environ. Sci.*, 2024, **138**, 450–457.

12 M. C. Ozcan, P. Degirmencioglu, E. Ekinci, B. P. Karaman, K. Murtezaoglu and N. Oktar, *Appl. Catal., A*, 2024, **683**, 119850.

13 N. Altunay, M. F. Lanjwani, H. U. Haq, M. Tuzen and A. Elik, *Sustainable Chem. Pharm.*, 2024, **38**, 101464.

14 J. Arshad, F. M. A. Alzahrani, S. Munir, U. Younis, M. S. Al-Buriahi, Z. A. Alrowaili and M. F. Warsi, *Ceram. Int.*, 2023, **49**, 18988–19002.

15 F. M. A. Alzahran, J. Arshad, M. S. Al-Buriahi, Z. A. Alrowaili and S. Munir, *J. Taibah Univ. Sci.*, 2023, **17**, 2209676.

16 T. Velegraki, G. Balayiannis, E. Diamadopoulos, A. Katsaounis and D. Mantzavinos, *Chem. Eng. J.*, 2010, **160**, 538–548.

17 A. Arts, K. P. van den Berg, M. T. de Groot and J. van der Schaaf, *Curr. Res. Green Sustainable Chem.*, 2021, **4**, 100217.

18 H. Qin, R. Xiao, Y. Wang and H. Li, *Acta Sci. Circumstantiae*, 2019, **39**, 3786–3793.

19 L. Fijołek and L. Wolski, *Sci. Rep.*, 2022, **12**, 9043.

20 D. Franco Peláez, J. L. Rodríguez S, T. Poznyak, H. Martínez Gutiérrez, J. A. Andraca Adame, L. Lartundo Rojas and C. J. Ramos Torres, *RSC Adv.*, 2024, **14**, 3923–3935.

21 Z. Wang, X. Lin, Y. Huang and L. Ma, *J. Hazard. Mater.*, 2022, **431**, 128620.

22 H. Li, D. H. Wang and S. Hui, *Appl. Surf. Sci.*, 2021, **569**, 150994.

23 J. Xiang, L. Wang, F. Cao, K. Qian, S. Su, S. Hu, Y. Wang and L. Liu, *Chem. Eng. J.*, 2016, **302**, 570–576.

24 L. Cheng, S. Sin, J. Ji, S. Yang, C. Tan, Z. Gu, W. Song, C. Huang, C. Sun, C. Tang and L. Dong, *Fuel*, 2023, **342**, 127772.

25 J. Yang, S. Ren, B. Su, Y. zhou, G. Hu, L. Jiang, J. Cao, W. Liu, L. Yao, M. Kong, J. Yang and Q. Liu, *Catal. Lett.*, 2021, **151**, 2964–2971.

26 Y. Huang, L.-c. Nengzi, X. Zhang, J. Gou, Y. Gao, G. Zhu, Q. Cheng and X. Cheng, *Chem. Eng. J.*, 2020, **388**, 124274.

27 P. Dutta, S. Pal, M. S. Seehra, Y. C. Shi, A. Eyring and R. D. Ernst, *Chem. Mater.*, 2006, **18**, 5144–5146.

28 C. Chen, Y. Li, W. Ma, S. Guo, Q. Wang and Q. X. Li, *Sep. Purif. Technol.*, 2017, **183**, 1–10.

29 S. Dey and V. V. Praveen Kumar, *Curr. Res. Green Sustainable Chem.*, 2020, **3**, 100012.

30 H. Zheng, T. Guo, Z. Li, F. Meng and Y. Qin, *Chin. J. Inorg. Chem.*, 2013, **29**, 2575–2581.

31 G. Gao, J.-W. Shi, C. Liu, C. Gao, Z. Fan and C. Niu, *Appl. Surf. Sci.*, 2017, **411**, 338–346.

32 Y. Zhang, Z. Zeng, Y. Li, Y. Hou, J. Hu and Z. Huang, *Fuel*, 2021, **288**, 119700.

33 M. Wang, X. Hong, J. Chen, J. Li, X. Chen, J. Mi, Z. Liu and S. Xiong, *Chem. Eng. J.*, 2022, **440**, 135854.

34 E. Yadav, P. Ghising, K. Rajeev and Z. Hossain, *Phys. Rev. B*, 2023, **107**, 214446.

35 I. Arora and P. Kumar, *J. Mater. Sci.: Mater. Electron.*, 2020, **31**, 12725–12734.

36 E. A. Arkhipova, A. S. Ivanov, K. I. Maslakov, R. Y. Novotortsev, S. V. Savilov, H. Xia and S. M. Aldoshin, *Ionics*, 2024, **30**, 1125–1136.

37 B. Zhang, P. Liang, X. Zhang, J. Wang, C. Zhang, M. Xiong and X. He, *J. Colloid Interface Sci.*, 2024, **660**, 703–715.

38 C. Chen, H. Xie, P. He, X. Liu, C. Yang, N. Wang and C. Ge, *Appl. Surf. Sci.*, 2022, **571**, 151285.

39 P. Li, Z. Song, M. Yang, S. Chen, X. Xiao, W. Duan, L. Li and X. Huang, *Anal. Chem.*, 2020, **92**, 16089–16096.

40 W. Chen, R. Ran, D. Weng, X. Wu, J. Zhong and S. Han, *J. Rare Earths*, 2017, **35**, 970–976.

41 K. Reed, A. Cormack, A. Kulkarni, M. Mayton, D. Sayle, F. Klaessig and B. Stadler, *Environ. Sci.: Nano*, 2014, **1**, 390–405.

42 W. Hong, M. Shao, T. Zhu, H. Wang, Y. Sun, F. Shen and X. Li, *Appl. Catal., B*, 2020, **274**, 119088.

43 L. Lan, H. Gengshen, L. Jiqing and L. Mengfei, *Acta Phys.-Chim. Sin.*, 2012, **28**, 1012–1020.

44 S. Shao, D. Lei, Y. Song, L. Liang, Y. Liu and W. Jiao, *Ind. Eng. Chem. Res.*, 2021, **60**, 2123–2135.

45 X. Wei, S. Shao, X. Ding, W. Jiao and Y. Liu, *J. Cleaner Prod.*, 2020, **248**, 119179.

46 Y. Xu, Q. Wang, B. A. Yoza, Q. X. Li, Y. Kou, Y. Tang, H. Ye, Y. Li and C. Chen, *Front. Chem.*, 2019, **7**, 384.

47 L. Zhao, W. Ma, S. Lu and J. Ma, *Sep. Purif. Technol.*, 2019, **210**, 167–174.

48 Y. Wang, W. Yang, X. Yin and Y. Liu, *J. Environ. Chem. Eng.*, 2016, **4**, 3415–3425.

49 S. Afzal, X. Quan and S. Lu, *Appl. Catal., B*, 2019, **248**, 526–537.

50 Y. Liao, M. Fu, L. Chen, J. Wu, B. Huang and D. Ye, *Catal. Today*, 2013, **216**, 220–228.

51 R. Radhakrishnan, S. T. Oyama, J. G. Chen and K. Asakura, *J. Phys. Chem. B*, 2001, **105**, 4245–4253.

52 L. Zhao, J. Ma, Z. Sun and H. Liu, *Appl. Catal., B*, 2009, **89**, 326–334.

53 X. Weng, P. Sun, Y. Long, Q. Meng and Z. Wu, *Environ. Sci. Technol.*, 2017, **51**, 8057–8066.

54 M. Digne, P. Sautet, P. Raybaud, P. Euzen and H. Toulhoat, *J. Catal.*, 2004, **226**, 54–68.